The Astrophysical Journal Letters, 945:L6 (11pp), 2023 March 1 https://doi.org/10.3847/2041-8213/acba8c

Discovery of the Exceptionally Short Period Ultracool Dwarf Binary LP 413-53AB

Chih-Chun Hsu[1,2], Adam J. Burgasser[2], and Christopher A. Theissen[2,3]
[1] Center for Interdisciplinary Exploration and Research in Astrophysics (CIERA), Northwestern University, 1800 Sherman, Evanston, IL 60201, USA
chsu@northwestern.edu
[2] Center for Astrophysics and Space Science, University of California San Diego, La Jolla, CA 92093, USA
Received 2023 January 14; revised 2023 February 8; accepted 2023 February 8; published 2023 March 1

Abstract

We report the detection of large-amplitude, rapid radial velocity (RV) variations and line-splitting in high-resolution Keck/NIRSPEC spectra of the M9 dwarf LP 413-53. We attribute these features to binary motion. Analyzing data spanning 15 yr, we infer a preliminary orbital period of 0.7106156 ± 0.0000002 days, an eccentricity of 0.0088 ± 0.0017, a primary RV semiamplitude of $23.70 \pm 0.05\,\mathrm{km\,s^{-1}}$, and a secondary RV semiamplitude of $28.41 \pm 0.06\,\mathrm{km\,s^{-1}}$, implying a system mass ratio $M_{\mathrm{secondary}}/M_{\mathrm{primary}} = 0.8340 \pm 0.0017$. These measurements identify LP 413-53 as the shortest-period ultracool binary discovered to date, and one of the smallest separation main-sequence binaries known. The position and velocity of the system rule out previously reported membership in the Hyades Moving Group, and indicate that this is likely a pair of evolved (age $\gtrsim$1 Gyr), very-low-mass stars. Assuming masses consistent with evolved late-M and L dwarfs, we estimate an orbital separation of 0.0081–0.0084 au or 17–19 stellar radii, and an orbital inclination angle of 24°, making it unlikely that this system exhibits eclipse events. The larger radii of these stars at young ages would have put them near contact at the system's current separation, and we speculate that this system has undergone dynamical evolution, either through orbital angular momentum loss or ejection of a third component followed by tidal circularization. While further observations are needed to fully constrain the orbital and physical parameters of LP 413-53, this ultra-short-period ultracool dwarf binary system serves as a new test bed for formation and dynamical evolution models of very-low-mass multiples.

Unified Astronomy Thesaurus concepts: Close binary stars (254); M dwarf stars (982); Spectroscopic binary stars (1557); Low mass stars (2050); High resolution spectroscopy (2096)

1. Introduction

Multiple systems are fundamental in studies of star formation, evolution, and physical characterization. These systems can provide direct measurements of stellar mass, while observed distributions of orbital separation, period, mass ratio, and eccentricity constrain star formation theory. The closest-separation systems are particularly useful given their short orbital cadence and the opportunity to measure both masses and radii through mutual eclipses, essential for calibrating stellar evolution and structure models.

The frequency of stellar multiplicity is known to scale with system mass, with the binary fraction declining from >80% for the most massive O-type stars to <20% for the lowest-mass stars and brown dwarfs (Duchene & Kraus 2013 and references therein). The latter ultracool dwarf (UCD) binaries ($M < 0.1\,M_{\odot}$) also have smaller orbital separations and eccentricities, and higher secondary-to-primary mass ratios, compared to solar-type stars (Burgasser et al. 2007; Dupuy & Liu 2017; Fontanive et al. 2018). The majority of UCD binaries have been discovered as resolved systems, while the most closely separated binaries have been identified as overluminous sources (Smart et al. 2019), spectral blend binaries (Burgasser et al. 2010; Bardalez Gagliuffi et al. 2014), and astrometric or radial velocity (RV) variables (Basri & Martin 1999; Blake et al. 2010; Sahlmann et al. 2020; Hsu et al. 2021a). Only three eclipsing UCD binaries have so far been reported in the literature: 2MASS J0535−0546AB (Stassun et al. 2006), USCO J1616−2512 (Lodieu et al. 2015), and SPEC J1510−2818AB (Triaud et al. 2020), the second of these having the shortest period at 2.8 days. For comparison, the closest-separation (non-UCD) binaries have periods down to 0.2 days (Maceroni & Rucinski 1997; Dimitrov & Kjurkchieva 2010; Nefs et al. 2012; Davenport et al. 2013; Zhang et al. 2019). The three known eclipsing UCD binaries are all members of young star-forming regions and associations (1–40 Myr) and have inflated radii consistent with ongoing contraction. No fully evolved UCD eclipsing binary has been identified to date, although several transiting UCD companions to more massive stars have been found by missions such as the Transiting Exoplanet Survey Satellite (TESS; Ricker et al. 2016; Carmichael et al. 2021).

LP 413-53 (aka 2MASS J03505737+1818069) is an M9 dwarf (Gizis et al. 2000) that has exhibited multiple signs of unresolved multiplicity in observations conducted over the past 20 years. Its Gaia Data Release 3 (DR3; Gaia Collaboration et al. 2022) absolute G-band magnitude, $M_G = 14.376 \pm 0.010$, is nearly a full magnitude brighter than other M9 dwarfs (15.3 ± 0.5; Kiman et al. 2019), while its Gaia Renormalized Unit Weight Error (RUWE) value of 1.35 is in the range where binary-induced astrometric variability is likely (Belokurov et al. 2020). Reid et al. (2002) obtained high-resolution optical spectroscopy of LP 413-53 and reported a complex Hα emission feature, consisting of a narrow spike on top of a broad peak. The RV inferred from the peak of the Hα line ($5.8 \pm 2.0\,\mathrm{km\,s^{-1}}$) was inconsistent with other spectral features ($-14.3 \pm 0.4\,\mathrm{km\,s^{-1}}$). While it was noted that this behavior

[3] NASA Sagan Fellow.

was similar to that of a known Hyades double-lined spectroscopic binary (SB2), the authors ultimately concluded that they had captured a flare during the observation. Deshpande et al. (2012) obtained high-resolution near-infrared spectroscopy of LP 413-53 and reported an RV of $32.2 \pm 1.8\,\mathrm{km\,s^{-1}}$, discrepant with both measurements from Reid et al. (2002). In addition to the complex Hα emission morphology reported by Reid et al. (2002), this source exhibits long-term emission variability, with equivalent widths ranging from undetectable (<1 Å; Gizis et al. 2000) to typical for a late-type M dwarf (13 Å; Cruz & Reid 2002) to unusually high (40 Å; Reid et al. 2002). This variability could be an indicator of youth, and LP 413-53 has been reported as a possible kinematic member of the ∼650 Myr Hyades cluster (Goldman et al. 2013; Lodieu 2020). High-angular-resolution imaging observations obtained with the Hubble Space Telescope (Bouy et al. 2003; Gizis et al. 2003) and ground-based adaptive optics (Close et al. 2003) have failed to detect a companion down to 0.″1 (∼4 au), and no comoving companion is present in Gaia data out to a radius of 1°.

In this Letter, we report new high-resolution spectra of LP 413-53 that show line-doubling and large-amplitude RV variations, identifying this source as the shortest-period UCD binary discovered to date. In Section 2, we describe our spectroscopic observations of LP 413-53. In Section 3, we determine RVs through forward modeling using a two-star model, which confirm the binary nature of the system. In Section 4, we conduct orbit fits to our RV time series to determine orbital and physical parameters. In Section 5, we discuss the properties of this system and comment on its formation and dynamical evolution.

2. Observations

2.1. Keck/NIRSPEC

We obtained high-resolution near-infrared spectra of LP 413-53 using the Near-InfraRed SPECtrometer (NIRSPEC; McLean et al. 1998) on the Keck II telescope. Data were obtained in five UT epochs: 2022 March 13, 2022 July 10, 2022 October 16, 2022 December 2, and 2023 January 8. The first four nights had clear conditions with 0.″5–0.″6 seeing , while the last night had 1.″0 seeing. In July, we used the NIRSPEC-7 filter and 0.″432 $\times 12''$ slit to obtain 1.84–2.63 μm spectra at a resolution of $\lambda/\Delta\lambda \approx 35{,}000$. We obtained four exposures of 450 s each in two AB nodding pair sequences. In the other epochs, we used the Kband-band new filter, which covers 1.91–2.55 μm and provides 20% higher throughput (J. Lyke 2022, private communication). In March, we used the $0.''432 \times 12''$ slit and obtained six exposures of 300 s each in three AB sequences. In October, we used the $0.''288 \times 12''$ slit to acquire slightly higher-resolution data ($\lambda/\Delta\lambda \approx 52{,}000$), and obtained 12 exposures of 300 s each in four ABBA sequences; the last exposure was rejected due to high sky background during sunrise. In December, we used the $0.''288 \times 12''$ slit and obtained 21 exposures of 300 s each in three ABBA sequences and an additional A nod position. In January, we used the $0.''432 \times 12''$ slit and obtained 57 exposures of 300 s each in 13 ABBA sequences, two AB sequences, and an additional B nod position. For all observations, we observed the A0 V stars HD 25175 or HD 174567 before or after our LP 413-53 exposures for telluric and wavelength calibration. We also obtained internal dark frame, flat-field lamp, and arc lamp exposures at the beginning or end of the night for detector calibration. Data were reduced using a modified version of the NIRSPEC Data Reduction Pipeline (Tran et al. 2016), as detailed in Theissen et al. (2022) and Hsu et al. (2021a). Median signals-to-noise (S/N) range from 6 to 30 per pixel (Table 1).

We also evaluated archival high-resolution NIRSPEC *J*-band spectra available on the Keck Observatory Archive (Tran et al. 2014),[4] obtained on 2007 October 26–27 (UT) through program 2007B-N076NS (PI E. Martín) and reported in Deshpande et al. (2012). We reanalyzed these data following the same procedures as our acquired data.

3. Radial Velocity Measurements

Figure 1 displays the sequence of NIRSPEC spectra of LP 413-53 from 2022 December 2, centered near $\lambda \sim 2.31$ μm, a region relatively free of telluric absorption. The data are initially consistent with a singled-line spectrum, but over the course of the sequence we observe double-line splitting, with the stronger line of each pair drifting to the right (positive velocity change) and the weaker line drifting to the left (negative velocity change). Similar behaviors are observed in the first four epochs of our acquired NIRSPEC data, while the last epoch showed the lines swapped and drifting in the opposite directions. Combined with the large variance of past RV measurements, we interpret these patterns as arising from the orbital motion of primary and secondary components in a close-separation binary.

To more precisely measure these trends in the NIRSPEC data, we used a Markov Chain Monte Carlo (MCMC) forward-modeling approach integrated in the `Spectral Modeling Analysis and RV Tool` (`SMART`) package (Hsu et al. 2021a, 2021b). This code fits individual "raw" (uncalibrated) high-resolution near-infrared spectra to infer RV, rotational velocity ($v \sin i$), temperature ($T_{\rm eff}$), and surface gravity ($\log g$), as well as several calibration parameters. For our acquired NIRSPEC observations, we focused our analysis on order 33 data, which covers the ^{12}CO ($\nu = 2$–0) bandhead (2.285–2.318 μm) in the stellar spectra, and the telluric CH_4 $\nu_2+\nu_3$ Q branch (McMath et al. 1949) at ∼2.315 μm, which anchors the absolute wavelength calibration. For the archival observations, we analyzed data in order 57, which covers wavelengths between 1.325 and 1.347 μm. We used BT-Settl atmosphere models (Allard et al. 2012) for the stellar components and ESO models for telluric absorption (Moehler et al. 2014). An initial fit assuming a single-star model was made to obtain a first estimate of the four physical parameters of the primary listed above, as well as the telluric airmass (AM) and precipitable water vapor (PWV). We then adapted the `SMART` code to implement a two-star model (see Triaud et al. 2020), with independent values of the physical parameters of each component (eight stellar parameters), their relative flux scaling f (one parameter), the telluric model (two parameters), and nuisance parameters (three parameters: flux, wavelength, and noise scale factor; see Hsu et al. 2021a for details).

MCMC modeling of each spectrum was done in two stages: an initial fit of the data was made to obtain preliminary parameters; a second fit of the data was then made after masking 2.5σ flux outliers, which typically removes bad pixels. Each MCMC run was conducted with 50 chains and 1000 steps, with

[4] https://koa.ipac.caltech.edu/

Table 1
NIRSPEC Measurements

				Primary				Secondary						
UT Date	MJD (TDB)[a]	S/N	Order	$T_{\rm eff}$ (K)	$\log g$ (cm s^{-2})	RV (km s^{-1})	$v \sin i$ (km s^{-1})	$T_{\rm eff}$ (K)	$\log g$ (cm s^{-2})	RV (km s^{-1})	$v \sin i$ (km s^{-1})	$C_{\rm scale}$[b]	χ_r^2[c]	$\chi^2_{r,s}$[c,d]
2007 Oct 26[e]	54,399.55066	18.8	57	3027^{+40}_{-42}	$4.74^{+0.26}_{-0.38}$	$-11.43^{+0.25}_{-0.23}$	$4.3^{+1.14}_{-1.33}$	2858^{+50}_{-100}	$4.74^{+0.26}_{-0.39}$	$33.94^{+0.58}_{-0.4}$	$5.14^{+1.88}_{-2.22}$	$0.55^{+0.05}_{-0.05}$	2.6	4.4
2007 Oct 26[e]	54,399.55441	19.1	57	3001^{+33}_{-32}	$4.88^{+0.2}_{-0.2}$	$-10.8^{+0.29}_{-0.22}$	$4.11^{+1.02}_{-2.25}$	2962^{+50}_{-62}	$4.88^{+0.42}_{-0.44}$	$33.57^{+0.35}_{-0.34}$	$3.1^{+1.78}_{-1.57}$	$0.56^{+0.05}_{-0.04}$	2.6	4.1
2007 Oct 27[e]	54,400.59805	16.5	57	2944^{+37}_{-38}	$5.42^{+0.05}_{-0.08}$	$31.4^{+0.35}_{-0.25}$	$4.43^{+1.16}_{-1.18}$	2978^{+76}_{-72}	$5.42^{+0.24}_{-0.23}$	$-17.36^{+0.48}_{-0.55}$	$6.93^{+1.07}_{-1.6}$	$0.68^{+0.05}_{-0.06}$	2.4	3.8
2007 Oct 27[e]	54,400.60189	16.5	57	2920^{+37}_{-32}	$4.91^{+0.2}_{-0.18}$	$30.89^{+0.29}_{-0.27}$	$5.21^{+1.67}_{-1.42}$	2924^{+60}_{-74}	$4.91^{+0.43}_{-0.44}$	$-17.64^{+0.41}_{-0.46}$	$3.57^{+1.59}_{-1.65}$	$0.64^{+0.06}_{-0.05}$	2.5	4.1
2022 Mar 13	59,651.20897	22.3	33	2895^{+15}_{-11}	$5.49^{+0.01}_{-0.01}$	$23.84^{+0.13}_{-0.16}$	$6.55^{+0.42}_{-0.52}$	2617^{+36}_{-35}	$5.49^{+0.02}_{-0.03}$	$-13.04^{+0.28}_{-0.27}$	$4.56^{+0.9}_{-1.28}$	$0.57^{+0.01}_{-0.01}$	2.7	7.6
2022 Mar 13	59,651.21244	24.2	33	2861^{+14}_{-12}	$5.49^{+0.0}_{-0.01}$	$24.43^{+0.14}_{-0.14}$	$6.72^{+0.32}_{-0.62}$	2639^{+36}_{-31}	$5.49^{+0.01}_{-0.02}$	$-13.83^{+0.16}_{-0.17}$	$3.31^{+1.21}_{-1.86}$	$0.57^{+0.01}_{-0.01}$	3.0	9.1
2022 Mar 13	59,651.24995	29.2	33	2893^{+12}_{-12}	$5.49^{+0.01}_{-0.01}$	$28.22^{+0.12}_{-0.11}$	$5.49^{+0.71}_{-0.7}$	2604^{+35}_{-38}	$5.49^{+0.03}_{-0.07}$	$-18.75^{+0.24}_{-0.23}$	$6.61^{+0.86}_{-0.73}$	$0.6^{+0.01}_{-0.01}$	3.6	10.9
2022 Mar 13	59,651.25342	29.9	33	2874^{+11}_{-12}	$5.5^{+0.0}_{-0.01}$	$28.5^{+0.16}_{-0.12}$	$6.41^{+0.21}_{-0.64}$	2631^{+30}_{-33}	$5.5^{+0.01}_{-0.01}$	$-19.82^{+0.2}_{-0.22}$	$6.95^{+0.9}_{-0.93}$	$0.6^{+0.02}_{-0.01}$	4.0	11.6
2022 Mar 13	59,651.26251	22.8	33	2905^{+18}_{-17}	$5.49^{+0.02}_{-0.01}$	$29.07^{+0.14}_{-0.2}$	$6.66^{+0.33}_{-0.48}$	2645^{+40}_{-37}	$5.49^{+0.03}_{-0.04}$	$-20.52^{+0.3}_{-0.27}$	$4.59^{+0.97}_{-2.2}$	$0.58^{+0.02}_{-0.02}$	2.8	7.5
2022 Mar 13	59,651.26598	22.5	33	2883^{+13}_{-13}	$5.49^{+0.01}_{-0.01}$	$29.31^{+0.16}_{-0.18}$	$5.26^{+0.5}_{-0.52}$	2615^{+28}_{-33}	$5.49^{+0.02}_{-0.03}$	$-20.68^{+0.22}_{-0.25}$	$6.3^{+1.2}_{-1.31}$	$0.61^{+0.02}_{-0.02}$	2.9	7.4
2022 Jul 10	59,770.61234	9.7	33	2892^{+31}_{-28}	$5.48^{+0.02}_{-0.04}$	$25.69^{+0.27}_{-0.24}$	$8.29^{+0.87}_{-0.95}$	2519^{+88}_{-79}	$5.24^{+0.19}_{-0.19}$	$-17.25^{+0.49}_{-0.3}$	$8.0^{+2.36}_{-2.16}$	$0.6^{+0.05}_{-0.03}$	1.8	3.0
2022 Jul 10	59,770.61755	14.8	33	2888^{+22}_{-22}	$5.48^{+0.01}_{-0.02}$	$26.59^{+0.23}_{-0.22}$	$7.47^{+0.61}_{-0.74}$	2639^{+34}_{-48}	$5.46^{+0.03}_{-0.05}$	$-17.96^{+0.34}_{-0.31}$	$4.63^{+1.71}_{-1.57}$	$0.6^{+0.03}_{-0.02}$	2.2	4.6
2022 Jul 10	59,770.62439	14.8	33	2884^{+26}_{-17}	$5.48^{+0.01}_{-0.03}$	$27.06^{+0.16}_{-0.16}$	$7.2^{+0.69}_{-0.6}$	2579^{+50}_{-80}	$5.44^{+0.05}_{-0.05}$	$-18.76^{+0.28}_{-0.37}$	$6.39^{+1.44}_{-1.6}$	$0.63^{+0.02}_{-0.02}$	2.2	4.4
2022 Jul 10	59,770.62960	17.9	33	2880^{+21}_{-19}	$5.48^{+0.01}_{-0.03}$	$28.28^{+0.24}_{-0.19}$	$7.05^{+0.81}_{-0.92}$	2600^{+39}_{-41}	$5.45^{+0.03}_{-0.08}$	$-19.28^{+0.22}_{-0.24}$	$4.53^{+1.69}_{-1.67}$	$0.58^{+0.02}_{-0.02}$	2.6	4.0
2022 Oct 16	59,868.61253	22.3	33	2872^{+16}_{-15}	$5.49^{+0.01}_{-0.01}$	$15.41^{+0.16}_{-0.11}$	$5.09^{+0.39}_{-0.46}$	2642^{+40}_{-42}	$5.48^{+0.02}_{-0.03}$	$-3.97^{+0.21}_{-0.24}$	$2.86^{+1.19}_{-1.54}$	$0.57^{+0.03}_{-0.02}$	3.4	5.9
2022 Oct 16	59,868.61643	18.2	33	2867^{+18}_{-20}	$5.49^{+0.01}_{-0.02}$	$16.07^{+0.14}_{-0.14}$	$5.17^{+0.44}_{-0.53}$	2676^{+36}_{-38}	$5.47^{+0.02}_{-0.03}$	$-4.96^{+0.31}_{-0.27}$	$6.48^{+0.56}_{-0.98}$	$0.58^{+0.03}_{-0.02}$	2.7	5.0
2022 Oct 16	59,868.62050	23.8	33	2885^{+19}_{-20}	$5.49^{+0.01}_{-0.02}$	$17.07^{+0.16}_{-0.13}$	$5.19^{+0.29}_{-0.32}$	2638^{+49}_{-32}	$5.48^{+0.01}_{-0.03}$	$-5.74^{+0.23}_{-0.25}$	$3.9^{+1.46}_{-1.41}$	$0.6^{+0.03}_{-0.02}$	3.4	6.8
2022 Oct 16	59,868.62439	22.7	33	2910^{+16}_{-19}	$5.49^{+0.01}_{-0.01}$	$18.16^{+0.14}_{-0.13}$	$5.33^{+0.48}_{-0.65}$	2552^{+51}_{-37}	$5.48^{+0.01}_{-0.01}$	$-6.52^{+0.31}_{-0.25}$	$4.55^{+0.86}_{-1.21}$	$0.61^{+0.02}_{-0.02}$	3.4	8.6
2022 Oct 16	59,868.62843	21.1	33	2914^{+18}_{-11}	$5.49^{+0.01}_{-0.01}$	$18.47^{+0.15}_{-0.13}$	$4.48^{+0.74}_{-0.95}$	2588^{+36}_{-30}	$5.48^{+0.01}_{-0.03}$	$-7.48^{+0.2}_{-0.25}$	$6.31^{+1.11}_{-0.74}$	$0.65^{+0.02}_{-0.03}$	3.1	6.2
2022 Oct 16	59,868.63232	25.4	33	2977^{+15}_{-15}	$5.49^{+0.01}_{-0.01}$	$19.75^{+0.12}_{-0.16}$	$5.56^{+0.77}_{-0.76}$	2358^{+7}_{-18}	$5.47^{+0.02}_{-0.04}$	$-8.13^{+0.24}_{-0.26}$	$3.45^{+1.08}_{-1.41}$	$0.7^{+0.04}_{-0.02}$	3.6	10.2
2022 Oct 16	59,868.63638	20.4	33	2886^{+18}_{-17}	$5.49^{+0.01}_{-0.02}$	$19.96^{+0.21}_{-0.12}$	$5.77^{+0.76}_{-0.85}$	2603^{+50}_{-41}	$5.47^{+0.02}_{-0.03}$	$-9.51^{+0.19}_{-0.23}$	$4.29^{+1.27}_{-1.45}$	$0.62^{+0.02}_{-0.02}$	2.9	6.1
2022 Oct 16	59,868.64024	22.7	33	2901^{+19}_{-20}	$5.49^{+0.01}_{-0.01}$	$20.45^{+0.14}_{-0.1}$	$5.11^{+0.47}_{-0.33}$	2636^{+29}_{-46}	$5.49^{+0.01}_{-0.02}$	$-10.45^{+0.18}_{-0.22}$	$4.53^{+1.29}_{-1.03}$	$0.6^{+0.02}_{-0.01}$	3.2	7.7
2022 Oct 16	59,868.64550	14.4	33	2902^{+25}_{-38}	$5.47^{+0.02}_{-0.05}$	$21.57^{+0.31}_{-0.23}$	$6.08^{+0.62}_{-0.99}$	2560^{+72}_{-62}	$5.43^{+0.05}_{-0.07}$	$-11.7^{+0.36}_{-0.35}$	$6.68^{+1.51}_{-1.39}$	$0.66^{+0.02}_{-0.03}$	2.2	4.2
2022 Oct 16	59,868.64936	20.1	33	2919^{+18}_{-17}	$5.49^{+0.01}_{-0.02}$	$21.91^{+0.17}_{-0.13}$	$5.37^{+0.27}_{-0.53}$	2616^{+48}_{-42}	$5.48^{+0.01}_{-0.02}$	$-12.33^{+0.32}_{-0.25}$	$3.52^{+1.28}_{-1.54}$	$0.57^{+0.02}_{-0.02}$	2.8	6.7
2022 Oct 16[e]	59,868.66123	7.7	33	2955^{+29}_{-42}	$5.46^{+0.03}_{-0.06}$	$23.7^{+0.26}_{-0.17}$	$3.29^{+1.03}_{-1.4}$	2595^{+54}_{-71}	$5.43^{+0.05}_{-0.1}$	$-14.31^{+0.41}_{-0.4}$	$5.86^{+1.96}_{-1.8}$	$0.66^{+0.04}_{-0.04}$	1.5	2.4
2022 Dec 2[e]	59,915.47470	15.0	33	2930^{+28}_{-30}	$5.49^{+0.01}_{-0.02}$	$6.58^{+0.27}_{-0.26}$	$2.1^{+1.03}_{-1.27}$	2561^{+58}_{-94}	$5.49^{+0.01}_{-0.02}$	$7.47^{+0.58}_{-0.53}$	$9.36^{+0.46}_{-0.85}$	$0.85^{+0.1}_{-0.17}$	2.4	3.2
2022 Dec 2[e]	59,915.47817	12.7	33	2893^{+31}_{-36}	$5.49^{+0.01}_{-0.02}$	$6.7^{+0.57}_{-0.68}$	$5.95^{+0.83}_{-1.08}$	2621^{+66}_{-53}	$5.48^{+0.01}_{-0.03}$	$8.13^{+1.14}_{-0.97}$	$8.67^{+1.06}_{-2.11}$	$0.8^{+0.14}_{-0.2}$	2.0	2.4
2022 Dec 2[e]	59,915.48277	10.5	33	2911^{+50}_{-56}	$5.48^{+0.02}_{-0.03}$	$8.44^{+0.7}_{-0.78}$	$6.78^{+1.06}_{-0.84}$	2584^{+121}_{-113}	$5.47^{+0.02}_{-0.04}$	$4.44^{+1.53}_{-1.2}$	$8.65^{+1.1}_{-1.58}$	$0.75^{+0.16}_{-0.16}$	2.0	2.4
2022 Dec 2[e]	59,915.48624	9.2	33	2820^{+51}_{-41}	$5.48^{+0.01}_{-0.03}$	$10.11^{+0.62}_{-0.71}$	$7.67^{+1.29}_{-1.42}$	2737^{+45}_{-68}	$5.47^{+0.02}_{-0.05}$	$3.69^{+1.04}_{-1.08}$	$8.54^{+1.09}_{-1.84}$	$0.75^{+0.16}_{-0.17}$	1.6	2.0
2022 Dec 2	59,915.48637	15.7	33	2886^{+36}_{-34}	$5.48^{+0.01}_{-0.04}$	$11.97^{+0.39}_{-0.35}$	$3.94^{+1.21}_{-0.66}$	2649^{+50}_{-45}	$5.47^{+0.02}_{-0.03}$	$2.08^{+0.63}_{-0.58}$	$6.03^{+1.57}_{-1.34}$	$0.77^{+0.1}_{-0.16}$	2.0	2.5
2022 Dec 2	59,915.49048	14.2	33	2755^{+39}_{-31}	$5.48^{+0.02}_{-0.02}$	$12.14^{+0.47}_{-0.35}$	$6.26^{+1.09}_{-0.95}$	2818^{+62}_{-52}	$5.47^{+0.02}_{-0.04}$	$0.08^{+0.62}_{-0.51}$	$6.06^{+1.33}_{-1.38}$	$0.59^{+0.13}_{-0.07}$	2.1	2.6
2022 Dec 2	59,915.49841	13.3	33	2838^{+22}_{-22}	$5.48^{+0.01}_{-0.02}$	$12.56^{+0.24}_{-0.24}$	$4.34^{+0.88}_{-0.99}$	2671^{+57}_{-51}	$5.45^{+0.04}_{-0.06}$	$-0.87^{+0.43}_{-0.39}$	$4.44^{+1.7}_{-1.29}$	$0.54^{+0.06}_{-0.03}$	2.1	2.6
2022 Dec 2	59,915.50188	11.7	33	2865^{+32}_{-31}	$5.49^{+0.01}_{-0.01}$	$13.31^{+0.24}_{-0.22}$	$5.24^{+0.52}_{-0.73}$	2619^{+63}_{-75}	$5.48^{+0.02}_{-0.03}$	$-1.14^{+0.43}_{-0.38}$	$3.83^{+1.51}_{-2.11}$	$0.58^{+0.08}_{-0.04}$	1.8	2.3
2022 Dec 2	59,915.50612	10.8	33	2910^{+25}_{-35}	$5.48^{+0.02}_{-0.04}$	$14.46^{+0.22}_{-0.26}$	$4.86^{+0.73}_{-0.69}$	2605^{+67}_{-59}	$5.45^{+0.03}_{-0.05}$	$-2.3^{+0.36}_{-0.34}$	$2.68^{+1.44}_{-1.91}$	$0.57^{+0.04}_{-0.04}$	1.9	2.4
2022 Dec 2	59,915.50959	9.2	33	2833^{+29}_{-35}	$5.48^{+0.02}_{-0.03}$	$15.09^{+0.3}_{-0.31}$	$6.74^{+0.89}_{-0.81}$	2689^{+66}_{-58}	$5.46^{+0.03}_{-0.08}$	$-2.82^{+0.37}_{-0.4}$	$4.47^{+1.74}_{-1.24}$	$0.59^{+0.05}_{-0.04}$	1.8	2.3
2022 Dec 2	59,915.51409	17.5	33	2826^{+22}_{-23}	$5.49^{+0.01}_{-0.01}$	$15.77^{+0.22}_{-0.21}$	$6.05^{+0.59}_{-0.42}$	2724^{+35}_{-26}	$5.48^{+0.01}_{-0.03}$	$-4.45^{+0.28}_{-0.2}$	$5.19^{+0.92}_{-1.21}$	$0.6^{+0.02}_{-0.04}$	2.6	3.8
2022 Dec 2	59,915.51756	19.2	33	2872^{+18}_{-20}	$5.49^{+0.01}_{-0.02}$	$16.38^{+0.14}_{-0.11}$	$6.12^{+0.47}_{-0.83}$	2660^{+46}_{-52}	$5.48^{+0.02}_{-0.03}$	$-5.43^{+0.26}_{-0.26}$	$6.23^{+0.66}_{-0.8}$	$0.58^{+0.02}_{-0.02}$	2.6	4.4
2022 Dec 2	59,915.52637	19.8	33	2875^{+16}_{-20}	$5.47^{+0.02}_{-0.03}$	$17.5^{+0.15}_{-0.16}$	$4.93^{+0.58}_{-0.28}$	2637^{+43}_{-51}	$5.47^{+0.02}_{-0.04}$	$-5.67^{+0.28}_{-0.25}$	$2.48^{+1.58}_{-1.59}$	$0.55^{+0.02}_{-0.02}$	2.7	4.9
2022 Dec 2	59,915.52529	17.3	33	2824^{+24}_{-24}	$5.49^{+0.01}_{-0.02}$	$17.89^{+0.17}_{-0.14}$	$5.53^{+0.76}_{-0.78}$	2745^{+31}_{-42}	$5.48^{+0.02}_{-0.04}$	$-6.92^{+0.18}_{-0.27}$	$6.3^{+0.84}_{-0.79}$	$0.63^{+0.02}_{-0.03}$	2.7	4.6
2022 Dec 2	59,915.52973	17.7	33	2854^{+21}_{-18}	$5.48^{+0.01}_{-0.02}$	$18.74^{+0.14}_{-0.21}$	$6.17^{+0.42}_{-0.55}$	2722^{+39}_{-42}	$5.48^{+0.02}_{-0.04}$	$-7.71^{+0.32}_{-0.29}$	$5.92^{+0.87}_{-1.21}$	$0.59^{+0.02}_{-0.02}$	2.8	4.9
2022 Dec 2	59,915.53320	16.6	33	2876^{+19}_{-18}	$5.49^{+0.01}_{-0.02}$	$19.39^{+0.13}_{-0.11}$	$6.32^{+0.39}_{-0.53}$	2627^{+49}_{-41}	$5.47^{+0.02}_{-0.04}$	$-8.5^{+0.3}_{-0.25}$	$6.37^{+1.06}_{-0.85}$	$0.59^{+0.02}_{-0.02}$	2.3	4.5

Table 1
(Continued)

UT Date	MJD (TDB)[a]	S/N	Order	Primary $T_{\rm eff}$ (K)	Primary $\log g$ (cm s^{-2})	Primary RV (km s^{-1})	Primary $v \sin i$ (km s^{-1})	Secondary $T_{\rm eff}$ (K)	Secondary $\log g$ (cm s^{-2})	Secondary RV (km s^{-1})	Secondary $v \sin i$ (km s^{-1})	$C_{\rm scale}$[b]	χ^2_r[c]	$\chi^2_{r,s}$[c,d]
2022 Dec 2	59,915.53744	15.8	33	2858^{+23}_{-29}	$5.49^{+0.01}_{-0.02}$	$20.03^{+0.19}_{-0.13}$	$5.48^{+0.88}_{-0.66}$	2693^{+44}_{-58}	$5.48^{+0.02}_{-0.04}$	$-9.76^{+0.26}_{-0.27}$	$4.19^{+1.16}_{-1.82}$	$0.57^{+0.02}_{-0.02}$	2.1	4.4
2022 Dec 2	59,915.54091	14.5	33	2807^{+29}_{-24}	$5.49^{+0.01}_{-0.02}$	$20.8^{+0.18}_{-0.18}$	$6.66^{+0.6}_{-0.6}$	2705^{+53}_{-49}	$5.44^{+0.04}_{-0.05}$	$-10.74^{+0.34}_{-0.33}$	$7.95^{+1.0}_{-0.79}$	$0.62^{+0.03}_{-0.02}$	2.5	5.0
2022 Dec 2	59,915.54538	13.3	33	2799^{+26}_{-29}	$5.48^{+0.01}_{-0.02}$	$21.36^{+0.19}_{-0.18}$	$4.43^{+0.88}_{-1.04}$	2750^{+51}_{-42}	$5.46^{+0.03}_{-0.04}$	$-11.6^{+0.27}_{-0.3}$	$8.31^{+0.83}_{-0.77}$	$0.67^{+0.03}_{-0.03}$	2.3	4.3
2022 Dec 2	59,915.55387	13.6	33	2885^{+26}_{-20}	$5.49^{+0.01}_{-0.01}$	$22.12^{+0.14}_{-0.18}$	$5.51^{+0.85}_{-0.74}$	2608^{+51}_{-61}	$5.45^{+0.04}_{-0.04}$	$-12.2^{+0.38}_{-0.32}$	$4.54^{+1.37}_{-1.39}$	$0.55^{+0.02}_{-0.02}$	2.0	3.9
2022 Dec 2	59,915.55734	15.0	33	2926^{+24}_{-18}	$5.48^{+0.01}_{-0.02}$	$22.83^{+0.18}_{-0.22}$	$5.39^{+0.42}_{-0.59}$	2643^{+43}_{-50}	$5.47^{+0.02}_{-0.04}$	$-12.46^{+0.29}_{-0.29}$	$7.35^{+1.06}_{-1.06}$	$0.58^{+0.02}_{-0.02}$	2.3	5.1
2023 Jan 8	59,952.21939	23.6	33	2851^{+18}_{-16}	$5.49^{+0.01}_{-0.01}$	$-16.3^{+0.16}_{-0.17}$	$3.87^{+0.61}_{-0.87}$	2655^{+25}_{-27}	$5.47^{+0.02}_{-0.05}$	$34.47^{+0.23}_{-0.23}$	$5.24^{+1.33}_{-1.03}$	$0.67^{+0.02}_{-0.02}$	2.4	7.4
2023 Jan 8	59,952.22286	23.6	33	2817^{+18}_{-14}	$5.48^{+0.01}_{-0.02}$	$-16.53^{+0.2}_{-0.15}$	$3.79^{+0.64}_{-0.74}$	2671^{+27}_{-36}	$5.48^{+0.02}_{-0.03}$	$34.65^{+0.25}_{-0.25}$	$6.08^{+0.91}_{-1.28}$	$0.65^{+0.02}_{-0.02}$	2.5	6.5
2023 Jan 8	59,952.22707	21.3	33	2828^{+15}_{-19}	$5.49^{+0.01}_{-0.02}$	$-16.76^{+0.2}_{-0.18}$	$2.98^{+0.86}_{-1.36}$	2675^{+28}_{-29}	$5.47^{+0.02}_{-0.04}$	$35.22^{+0.22}_{-0.22}$	$6.46^{+0.91}_{-1.33}$	$0.65^{+0.02}_{-0.02}$	2.3	9.1
2023 Jan 8	59,952.23054	20.8	33	2855^{+18}_{-17}	$5.49^{+0.01}_{-0.02}$	$-16.95^{+0.21}_{-0.18}$	$2.85^{+1.08}_{-1.61}$	2677^{+29}_{-32}	$5.46^{+0.03}_{-0.06}$	$34.95^{+0.24}_{-0.31}$	$6.63^{+1.01}_{-0.84}$	$0.68^{+0.02}_{-0.02}$	2.2	8.1
2023 Jan 8	59,952.23504	19.9	33	2856^{+16}_{-19}	$5.49^{+0.01}_{-0.01}$	$-16.92^{+0.16}_{-0.17}$	$3.49^{+0.62}_{-1.21}$	2668^{+25}_{-36}	$5.48^{+0.01}_{-0.03}$	$34.89^{+0.31}_{-0.31}$	$4.58^{+1.22}_{-1.82}$	$0.65^{+0.02}_{-0.02}$	2.2	5.5
2023 Jan 8	59,952.23851	19.3	33	2846^{+19}_{-22}	$5.49^{+0.01}_{-0.02}$	$-17.11^{+0.18}_{-0.2}$	$1.81^{+1.23}_{-0.99}$	2709^{+27}_{-40}	$5.47^{+0.02}_{-0.04}$	$35.03^{+0.4}_{-0.4}$	$6.22^{+1.19}_{-1.53}$	$0.67^{+0.03}_{-0.02}$	2.2	4.8
2023 Jan 8	59,952.24275	17.2	33	2835^{+19}_{-22}	$5.48^{+0.01}_{-0.02}$	$-17.0^{+0.22}_{-0.24}$	$3.34^{+0.98}_{-1.32}$	2646^{+40}_{-33}	$5.47^{+0.02}_{-0.04}$	$35.45^{+0.36}_{-0.42}$	$6.25^{+1.46}_{-1.41}$	$0.65^{+0.02}_{-0.02}$	2.2	6.3
2023 Jan 8	59,952.24622	15.9	33	2867^{+19}_{-14}	$5.48^{+0.01}_{-0.03}$	$-16.78^{+0.18}_{-0.18}$	$4.54^{+0.92}_{-1.0}$	2638^{+40}_{-38}	$5.46^{+0.03}_{-0.06}$	$35.83^{+0.37}_{-0.37}$	$5.71^{+1.15}_{-1.16}$	$0.62^{+0.03}_{-0.02}$	2.1	4.5
2023 Jan 8	59,952.26061	17.1	33	2864^{+18}_{-18}	$5.49^{+0.01}_{-0.02}$	$-16.43^{+0.19}_{-0.18}$	$5.05^{+0.62}_{-0.59}$	2632^{+34}_{-33}	$5.46^{+0.03}_{-0.05}$	$34.88^{+0.28}_{-0.34}$	$6.27^{+0.84}_{-1.1}$	$0.66^{+0.02}_{-0.02}$	2.2	5.5
2023 Jan 8	59,952.26408	19.6	33	2830^{+19}_{-17}	$5.48^{+0.01}_{-0.02}$	$-16.45^{+0.16}_{-0.12}$	$3.65^{+0.75}_{-1.39}$	2678^{+29}_{-33}	$5.48^{+0.01}_{-0.03}$	$33.96^{+0.45}_{-0.46}$	$7.5^{+0.83}_{-1.21}$	$0.65^{+0.02}_{-0.02}$	2.1	4.7
2023 Jan 8	59,952.26863	17.6	33	2854^{+18}_{-20}	$5.48^{+0.01}_{-0.03}$	$-16.07^{+0.2}_{-0.22}$	$3.75^{+1.04}_{-1.44}$	2660^{+31}_{-39}	$5.46^{+0.03}_{-0.04}$	$33.96^{+0.25}_{-0.4}$	$6.53^{+1.3}_{-1.28}$	$0.67^{+0.02}_{-0.03}$	2.1	6.4
2023 Jan 8	59,952.27210	17.4	33	2848^{+14}_{-16}	$5.49^{+0.01}_{-0.01}$	$-15.84^{+0.18}_{-0.18}$	$3.02^{+1.02}_{-1.16}$	2689^{+19}_{-26}	$5.48^{+0.02}_{-0.03}$	$33.97^{+0.25}_{-0.31}$	$6.13^{+0.98}_{-1.19}$	$0.64^{+0.02}_{-0.02}$	2.3	5.8
2023 Jan 8	59,952.27630	20.0	33	2835^{+22}_{-15}	$5.49^{+0.01}_{-0.01}$	$-15.86^{+0.27}_{-0.21}$	$3.75^{+1.26}_{-0.82}$	2682^{+25}_{-39}	$5.48^{+0.02}_{-0.02}$	$33.6^{+0.25}_{-0.25}$	$5.01^{+1.24}_{-1.54}$	$0.65^{+0.02}_{-0.02}$	3.3	8.4
2023 Jan 8	59,952.27977	24.3	33	2858^{+13}_{-16}	$5.49^{+0.01}_{-0.01}$	$-15.57^{+0.14}_{-0.14}$	$3.86^{+0.62}_{-1.34}$	2660^{+28}_{-34}	$5.46^{+0.03}_{-0.04}$	$33.6^{+0.25}_{-0.32}$	$7.71^{+0.73}_{-0.9}$	$0.68^{+0.02}_{-0.02}$	2.6	7.4
2023 Jan 8	59,952.28447	23.9	33	2891^{+27}_{-19}	$5.49^{+0.01}_{-0.02}$	$-15.88^{+0.26}_{-0.23}$	$3.16^{+1.08}_{-1.41}$	2622^{+49}_{-39}	$5.45^{+0.03}_{-0.07}$	$32.28^{+0.3}_{-0.34}$	$5.01^{+1.57}_{-1.86}$	$0.66^{+0.02}_{-0.03}$	3.1	10.3
2023 Jan 8	59,952.28794	23.8	33	2870^{+18}_{-16}	$5.49^{+0.01}_{-0.02}$	$-15.4^{+0.17}_{-0.22}$	$4.13^{+1.04}_{-0.87}$	2638^{+34}_{-34}	$5.48^{+0.02}_{-0.03}$	$32.05^{+0.34}_{-0.46}$	$3.97^{+1.55}_{-1.82}$	$0.66^{+0.02}_{-0.02}$	2.3	5.5
2023 Jan 8	59,952.29219	18.5	33	2800^{+55}_{-47}	$5.3^{+0.1}_{-0.1}$	$-15.85^{+0.55}_{-0.57}$	$1.07^{+1.36}_{-0.78}$	2749^{+67}_{-89}	$5.39^{+0.07}_{-0.17}$	$29.77^{+0.35}_{-0.4}$	$4.13^{+2.25}_{-2.4}$	$0.67^{+0.05}_{-0.05}$	2.1	3.0
2023 Jan 8	59,952.29566	11.5	33	2835^{+45}_{-45}	$5.4^{+0.08}_{-0.13}$	$-14.82^{+0.59}_{-0.72}$	$4.96^{+1.88}_{-1.74}$	2614^{+64}_{-86}	$5.3^{+0.12}_{-0.18}$	$31.48^{+0.83}_{-0.83}$	$2.46^{+2.35}_{-1.82}$	$0.71^{+0.05}_{-0.05}$	1.7	2.0
2023 Jan 8	59,952.30045	5.9	33	2910^{+45}_{-40}	$5.45^{+0.04}_{-0.1}$	$-14.06^{+0.32}_{-0.28}$	$2.28^{+1.83}_{-1.2}$	2585^{+71}_{-85}	$5.31^{+0.15}_{-0.13}$	$31.98^{+0.58}_{-0.58}$	$3.81^{+2.44}_{-2.82}$	$0.7^{+0.04}_{-0.04}$	1.8	2.7
2023 Jan 8	59,952.30392	8.7	33	2889^{+19}_{-21}	$5.48^{+0.02}_{-0.03}$	$-13.65^{+0.19}_{-0.17}$	$3.93^{+1.26}_{-1.25}$	2569^{+11}_{-23}	$5.47^{+0.02}_{-0.03}$	$30.79^{+0.27}_{-0.27}$	$1.97^{+1.56}_{-1.09}$	$0.63^{+0.02}_{-0.02}$	2.9	5.7
2023 Jan 8	59,952.30816	19.2	33	2845^{+25}_{-39}	$5.48^{+0.02}_{-0.03}$	$-12.76^{+0.35}_{-0.25}$	$4.1^{+1.1}_{-1.25}$	2687^{+42}_{-44}	$5.42^{+0.05}_{-0.11}$	$31.34^{+0.45}_{-0.77}$	$2.88^{+2.05}_{-1.96}$	$0.62^{+0.04}_{-0.03}$	2.3	3.7
2023 Jan 8	59,952.31163	13.5	33	2908^{+30}_{-31}	$5.46^{+0.03}_{-0.06}$	$-12.36^{+0.26}_{-0.27}$	$4.82^{+0.88}_{-1.46}$	2582^{+63}_{-50}	$5.44^{+0.04}_{-0.05}$	$29.76^{+0.44}_{-0.46}$	$2.58^{+2.33}_{-1.79}$	$0.63^{+0.02}_{-0.02}$	2.5	4.5
2023 Jan 8	59,952.31611	16.3	33	2876^{+16}_{-23}	$5.48^{+0.01}_{-0.02}$	$-12.35^{+0.25}_{-0.23}$	$2.43^{+1.24}_{-1.44}$	2646^{+41}_{-48}	$5.46^{+0.02}_{-0.08}$	$28.59^{+0.3}_{-0.34}$	$4.4^{+1.7}_{-2.22}$	$0.65^{+0.02}_{-0.02}$	3.0	6.2
2023 Jan 8	59,952.31958	20.1	33	2864^{+22}_{-24}	$5.49^{+0.01}_{-0.02}$	$-11.55^{+0.32}_{-0.19}$	$2.05^{+1.16}_{-1.17}$	2665^{+43}_{-44}	$5.46^{+0.03}_{-0.05}$	$29.02^{+0.38}_{-0.38}$	$3.84^{+1.66}_{-1.71}$	$0.69^{+0.02}_{-0.02}$	2.7	5.8
2023 Jan 8	59,952.32379	17.4	33	2797^{+24}_{-21}	$5.49^{+0.01}_{-0.02}$	$-11.99^{+0.15}_{-0.17}$	$1.97^{+1.04}_{-1.12}$	2776^{+20}_{-8}	$5.48^{+0.02}_{-0.03}$	$27.35^{+0.34}_{-0.34}$	$6.82^{+1.27}_{-1.37}$	$0.72^{+0.04}_{-0.03}$	3.0	6.2
2023 Jan 8	59,952.32726	18.0	33	2881^{+16}_{-19}	$5.48^{+0.02}_{-0.03}$	$-10.64^{+0.17}_{-0.26}$	$2.32^{+0.85}_{-1.22}$	2640^{+32}_{-37}	$5.45^{+0.03}_{-0.06}$	$27.07^{+0.54}_{-0.54}$	$3.9^{+1.44}_{-1.68}$	$0.66^{+0.02}_{-0.02}$	2.7	7.5
2023 Jan 8	59,952.33181	22.3	33	2907^{+21}_{-27}	$5.47^{+0.02}_{-0.02}$	$-9.68^{+0.16}_{-0.21}$	$3.03^{+1.08}_{-1.04}$	2629^{+47}_{-51}	$5.46^{+0.02}_{-0.04}$	$26.35^{+0.37}_{-0.37}$	$3.63^{+1.89}_{-1.95}$	$0.64^{+0.02}_{-0.02}$	3.3	8.1
2023 Jan 8	59,952.33527	24.7	33	2878^{+15}_{-13}	$5.49^{+0.01}_{-0.01}$	$-9.16^{+0.18}_{-0.18}$	$2.17^{+0.83}_{-1.38}$	2604^{+32}_{-40}	$5.47^{+0.02}_{-0.04}$	$26.13^{+0.32}_{-0.32}$	$3.84^{+1.67}_{-1.8}$	$0.66^{+0.02}_{-0.02}$	2.5	5.9
2023 Jan 8	59,952.33951	19.1	33	2878^{+29}_{-21}	$5.48^{+0.02}_{-0.02}$	$-9.19^{+0.3}_{-0.34}$	$2.23^{+0.98}_{-1.22}$	2592^{+59}_{-56}	$5.45^{+0.03}_{-0.05}$	$24.84^{+0.31}_{-0.37}$	$5.54^{+1.75}_{-2.18}$	$0.68^{+0.02}_{-0.02}$	3.1	6.1
2023 Jan 8	59,952.34298	20.0	33	2883^{+16}_{-22}	$5.48^{+0.01}_{-0.02}$	$-8.22^{+0.25}_{-0.42}$	$4.23^{+1.03}_{-0.72}$	2572^{+48}_{-50}	$5.47^{+0.02}_{-0.03}$	$24.13^{+0.59}_{-0.59}$	$7.38^{+1.21}_{-1.07}$	$0.69^{+0.02}_{-0.02}$	3.1	6.7
2023 Jan 8	59,952.34754	23.2	33	2890^{+27}_{-18}	$5.49^{+0.01}_{-0.02}$	$-7.44^{+0.18}_{-0.19}$	$3.84^{+0.97}_{-0.63}$	2580^{+46}_{-48}	$5.47^{+0.02}_{-0.03}$	$23.92^{+0.41}_{-0.41}$	$7.57^{+1.42}_{-1.46}$	$0.68^{+0.02}_{-0.03}$	2.9	6.2
2023 Jan 8	59,952.35101	23.1	33	2864^{+28}_{-37}	$5.48^{+0.01}_{-0.03}$	$-6.32^{+0.18}_{-0.21}$	$1.02^{+0.97}_{-0.61}$	2622^{+67}_{-56}	$5.48^{+0.02}_{-0.04}$	$23.72^{+0.44}_{-0.44}$	$7.0^{+1.42}_{-1.54}$	$0.72^{+0.03}_{-0.03}$	3.0	5.3
2023 Jan 8	59,952.35525	20.1	33	2905^{+25}_{-25}	$5.49^{+0.01}_{-0.02}$	$-6.31^{+0.22}_{-0.31}$	$3.68^{+1.36}_{-0.87}$	2557^{+54}_{-51}	$5.47^{+0.02}_{-0.05}$	$21.59^{+0.35}_{-0.36}$	$6.93^{+2.18}_{-1.94}$	$0.7^{+0.03}_{-0.03}$	2.7	4.4
2023 Jan 8	59,952.35872	19.0	33	2889^{+15}_{-19}	$5.49^{+0.01}_{-0.01}$	$-5.89^{+0.19}_{-0.26}$	$4.31^{+0.95}_{-0.75}$	2528^{+48}_{-38}	$5.48^{+0.01}_{-0.03}$	$20.67^{+0.29}_{-0.34}$	$8.44^{+1.28}_{-1.23}$	$0.73^{+0.03}_{-0.02}$	2.4	4.3
2023 Jan 8	59,952.36321	20.4	33	2882^{+29}_{-28}	$5.49^{+0.01}_{-0.02}$	$-5.01^{+0.29}_{-0.42}$	$3.03^{+1.29}_{-1.58}$	2619^{+57}_{-66}	$5.49^{+0.01}_{-0.01}$	$19.64^{+0.35}_{-0.35}$	$8.8^{+1.25}_{-1.23}$	$0.73^{+0.03}_{-0.03}$	2.5	4.7
2023 Jan 8	59,952.36668	23.2	33	2897^{+21}_{-13}	$5.49^{+0.01}_{-0.01}$	$-3.98^{+0.17}_{-0.19}$	$1.51^{+1.09}_{-0.96}$	2545^{+33}_{-32}	$5.46^{+0.03}_{-0.04}$	$18.89^{+0.33}_{-0.33}$	$7.16^{+1.32}_{-1.39}$	$0.76^{+0.04}_{-0.03}$	3.0	4.5

Table 1
(Continued)

				Primary				Secondary						
UT Date	MJD (TDB)[a]	S/N	Order	$T_{\rm eff}$ (K)	log g (cm s^{-2})	RV (km s^{-1})	$v \sin i$ (km s^{-1})	$T_{\rm eff}$ (K)	log g (cm s^{-2})	RV (km s^{-1})	$v \sin i$ (km s^{-1})	$C_{\rm scale}$[b]	χ_r^2[c]	$\chi_{r,s}^2$[c,d]
2023 Jan 8	59,952.37092	21.0	33	2914^{+18}_{-18}	$5.49^{+0.01}_{-0.01}$	$-3.27^{+0.19}_{-0.19}$	$1.9^{+1.16}_{-1.16}$	2550^{+36}_{-42}	$5.46^{+0.02}_{-0.05}$	$18.09^{+0.3}_{-0.3}$	$6.79^{+1.02}_{-1.18}$	$0.73^{+0.03}_{-0.02}$	3.0	4.1
2023 Jan 8	59,952.37439	21.0	33	2936^{+29}_{-34}	$5.49^{+0.01}_{-0.01}$	$-2.93^{+0.25}_{-0.29}$	$2.45^{+1.45}_{-1.37}$	2527^{+42}_{-50}	$5.46^{+0.03}_{-0.04}$	$15.95^{+0.54}_{-0.7}$	$10.36^{+1.65}_{-1.44}$	$0.89^{+0.06}_{-0.06}$	2.4	3.0
2023 Jan 8	59,952.37893	18.8	33	2943^{+25}_{-34}	$5.48^{+0.01}_{-0.02}$	$-2.24^{+0.28}_{-0.2}$	$3.16^{+1.04}_{-1.22}$	2515^{+43}_{-68}	$5.46^{+0.03}_{-0.05}$	$15.48^{+0.41}_{-0.53}$	$10.69^{+1.31}_{-1.32}$	$0.94^{+0.04}_{-0.05}$	2.2	2.6
2023 Jan 8	59,952.38240	16.8	33	2923^{+25}_{-21}	$5.49^{+0.01}_{-0.01}$	$-1.21^{+0.24}_{-0.24}$	$1.5^{+1.13}_{-1.09}$	2535^{+38}_{-42}	$5.4^{+0.06}_{-0.09}$	$14.78^{+0.4}_{-0.41}$	$6.99^{+1.62}_{-1.7}$	$0.77^{+0.07}_{-0.05}$	2.5	2.9
2023 Jan 8	59,952.38664	18.9	33	2947^{+34}_{-22}	$5.49^{+0.01}_{-0.01}$	$-0.05^{+0.22}_{-0.21}$	$1.2^{+1.33}_{-0.88}$	2549^{+53}_{-48}	$5.46^{+0.03}_{-0.04}$	$13.97^{+0.52}_{-0.52}$	$6.97^{+1.9}_{-1.28}$	$0.87^{+0.07}_{-0.07}$	2.3	2.9
2023 Jan 8	59,952.39011	19.5	33	2888^{+26}_{-17}	$5.49^{+0.01}_{-0.01}$	$1.23^{+0.53}_{-0.38}$	$6.46^{+1.16}_{-0.95}$	2433^{+51}_{-82}	$5.43^{+0.05}_{-0.1}$	$14.56^{+0.75}_{-0.95}$	$4.38^{+1.77}_{-2.5}$	$0.59^{+0.08}_{-0.1}$	2.4	3.0
2023 Jan 8	59,952.39459	21.8	33	2908^{+29}_{-30}	$5.49^{+0.01}_{-0.01}$	$1.44^{+0.42}_{-0.55}$	$5.46^{+1.28}_{-1.47}$	2488^{+63}_{-68}	$5.48^{+0.01}_{-0.02}$	$13.04^{+0.98}_{-0.98}$	$2.75^{+2.68}_{-1.94}$	$0.65^{+0.11}_{-0.11}$	2.1	2.6
2023 Jan 8	59,952.39806	19.1	33	2939^{+19}_{-32}	$5.49^{+0.01}_{-0.02}$	$1.07^{+0.33}_{-0.27}$	$1.82^{+1.17}_{-1.11}$	2566^{+39}_{-58}	$5.47^{+0.02}_{-0.05}$	$10.78^{+0.33}_{-0.37}$	$1.69^{+1.97}_{-1.22}$	$0.92^{+0.05}_{-0.1}$	2.7	2.7
2023 Jan 8	59,952.40230	16.9	33	2890^{+49}_{-33}	$5.49^{+0.01}_{-0.01}$	$3.34^{+0.59}_{-0.57}$	$4.73^{+1.0}_{-1.28}$	2488^{+93}_{-88}	$5.47^{+0.02}_{-0.07}$	$11.41^{+1.26}_{-1.4}$	$2.93^{+2.8}_{-1.92}$	$0.65^{+0.26}_{-0.21}$	2.9	3.0
2023 Jan 8	59,952.40577	19.5	33	2889^{+28}_{-18}	$5.49^{+0.01}_{-0.01}$	$4.28^{+0.3}_{-0.39}$	$3.35^{+1.06}_{-1.17}$	2495^{+85}_{-74}	$5.47^{+0.02}_{-0.03}$	$9.76^{+1.11}_{-1.11}$	$10.75^{+1.51}_{-2.46}$	$0.64^{+0.18}_{-0.1}$	2.4	2.8
2023 Jan 8	59,952.41024	19.1	33	2890^{+31}_{-26}	$5.49^{+0.01}_{-0.02}$	$4.01^{+0.65}_{-0.44}$	$2.41^{+1.35}_{-1.77}$	2586^{+35}_{-49}	$5.48^{+0.02}_{-0.04}$	$9.01^{+0.86}_{-0.86}$	$7.73^{+3.01}_{-1.72}$	$0.73^{+0.15}_{-0.14}$	2.1	2.5
2023 Jan 8	59,952.41371	16.6	33	2887^{+25}_{-29}	$5.49^{+0.0}_{-0.02}$	$5.14^{+0.67}_{-0.74}$	$3.3^{+1.88}_{-1.79}$	2625^{+46}_{-38}	$5.49^{+0.01}_{-0.02}$	$7.98^{+1.02}_{-1.02}$	$4.53^{+2.94}_{-2.84}$	$0.83^{+0.09}_{-0.16}$	3.4	3.4
2023 Jan 8	59,952.41793	19.7	33	2875^{+30}_{-16}	$5.49^{+0.01}_{-0.01}$	$5.63^{+0.51}_{-0.7}$	$1.72^{+1.3}_{-1.25}$	2608^{+30}_{-24}	$5.49^{+0.01}_{-0.02}$	$7.55^{+0.94}_{-0.95}$	$6.41^{+1.8}_{-2.65}$	$0.72^{+0.2}_{-0.11}$	3.2	3.8
2023 Jan 8	59,952.42140	20.8	33	2847^{+29}_{-35}	$5.49^{+0.01}_{-0.02}$	$5.84^{+0.32}_{-0.61}$	$2.2^{+1.28}_{-1.2}$	2627^{+54}_{-50}	$5.48^{+0.02}_{-0.03}$	$7.8^{+0.76}_{-0.79}$	$10.06^{+1.6}_{-2.07}$	$0.72^{+0.15}_{-0.15}$	2.1	2.5
2023 Jan 8	59,952.42584	14.7	33	2869^{+28}_{-34}	$5.49^{+0.01}_{-0.02}$	$6.16^{+0.58}_{-0.77}$	$4.05^{+1.46}_{-2.08}$	2673^{+46}_{-53}	$5.49^{+0.01}_{-0.02}$	$6.9^{+0.78}_{-0.98}$	$6.53^{+2.08}_{-3.17}$	$0.77^{+0.15}_{-0.15}$	2.4	2.8
2023 Jan 8	59,952.42931	18.7	33	2881^{+27}_{-21}	$5.49^{+0.01}_{-0.02}$	$6.76^{+0.52}_{-0.43}$	$2.17^{+1.77}_{-1.37}$	2614^{+50}_{-34}	$5.49^{+0.01}_{-0.02}$	$6.21^{+0.85}_{-0.85}$	$7.89^{+1.55}_{-1.73}$	$0.87^{+0.1}_{-0.16}$	2.6	3.1
2023 Jan 8[e]	59,952.43355	19.1	33	2860^{+34}_{-34}	$5.49^{+0.01}_{-0.02}$	$7.06^{+0.59}_{-0.45}$	$5.13^{+1.73}_{-1.87}$	2657^{+57}_{-51}	$5.48^{+0.01}_{-0.03}$	$6.45^{+1.03}_{-1.03}$	$10.31^{+1.64}_{-1.92}$	$0.82^{+0.11}_{-0.16}$	2.4	2.9
2023 Jan 8[e]	59,952.43702	18.2	33	2904^{+30}_{-33}	$5.49^{+0.01}_{-0.01}$	$7.29^{+0.55}_{-0.85}$	$7.35^{+0.96}_{-1.46}$	2626^{+45}_{-47}	$5.49^{+0.01}_{-0.01}$	$6.49^{+0.74}_{-1.23}$	$10.18^{+1.8}_{-2.33}$	$0.84^{+0.11}_{-0.11}$	2.2	2.7
2023 Jan 8[e]	59,952.44147	19.1	33	2865^{+30}_{-29}	$5.49^{+0.01}_{-0.01}$	$7.47^{+0.75}_{-0.95}$	$9.73^{+1.54}_{-1.05}$	2633^{+52}_{-49}	$5.49^{+0.01}_{-0.02}$	$6.72^{+1.02}_{-1.43}$	$12.76^{+1.61}_{-2.07}$	$0.84^{+0.12}_{-0.16}$	1.9	2.3
2023 Jan 8	59,952.44954	17.6	33	2866^{+19}_{-22}	$5.48^{+0.02}_{-0.03}$	$11.52^{+0.35}_{-0.28}$	$5.72^{+1.03}_{-1.13}$	2534^{+78}_{-86}	$5.41^{+0.06}_{-0.1}$	$0.14^{+0.38}_{-0.46}$	$1.5^{+1.68}_{-1.06}$	$0.53^{+0.04}_{-0.02}$	2.5	2.5
2023 Jan 8	59,952.45301	16.7	33	2827^{+25}_{-23}	$5.49^{+0.01}_{-0.02}$	$12.92^{+0.33}_{-0.22}$	$2.25^{+1.19}_{-1.21}$	2697^{+38}_{-42}	$5.49^{+0.01}_{-0.02}$	$-0.4^{+0.4}_{-0.47}$	$2.7^{+2.27}_{-1.46}$	$0.68^{+0.09}_{-0.06}$	2.0	2.5
Average	⋯	⋯	⋯	2879 ± 37	5.49 ± 0.02	⋯	4.2 ± 1.7	2627 ± 71	5.47 ± 0.04	⋯	5.9 ± 2.0	0.65 ± 0.08	⋯	⋯

Notes.
[a] Modified Julian Dates with the Barycentric Dynamical Time correction included following Eastman et al. (2010).
[b] Flux scale for the secondary component.
[c] Reduced χ^2.
[d] Solution for the single star model.
[e] Epochs not included in parameter averages or orbit fits.

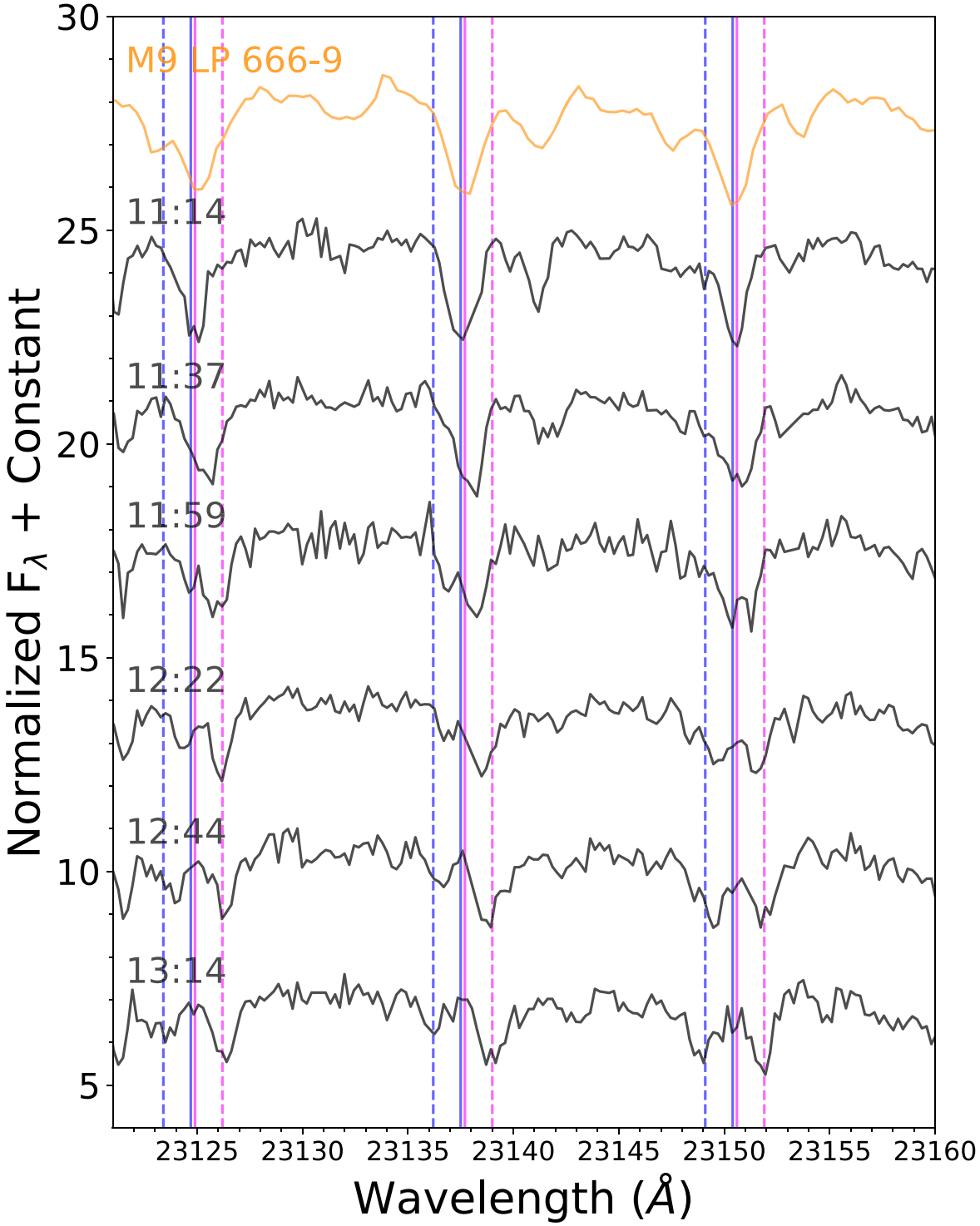

Figure 1. Sequence of LP 413-53 spectra over a 2 hr period on 2022 December 2 (UT), centered on the 2.312–2.316 μm region. Time increases from top to bottom, and UT times (hour and minute) are indicated next to each spectrum. The topmost spectrum shows equivalent data for the M9 dwarf LP 666-9 (C. Hsu et al. 2023, in preparation). Absorption features arising from CO are initially consistent with a single-line source, but become clearly doubled over the observing sequence, with the line centers of the stronger features drifting to the right and the line centers of the weaker features drifting to the left. Vertical lines mark line center positions at the start (solid) and end (dashed) of the sequence for the stronger (magenta) and weaker (blue) lines.

burn-ins of 600 and 500 steps for the initial and final fits, respectively. The best-fit parameters and associated uncertainties, determined from the 16%, 50%, and 84% quantiles of the chains after removing burn-in, are summarized in Table 1.

Figure 2 illustrates the best-fit model for data obtained on 2022 March 13 at 05:02:59.43 UT, or 59,651.20898 MJD.[5] The two-component model provides an excellent fit to the NIRSPEC spectrum, with flat residuals and a reduced

[5] All Modified Julian Dates (MJD) had the Barycentric Dynamical Time correction applied following Eastman et al. (2010) using the `JDUTC to BJDTDB` function in the `barycorrpy` package (Kanodia & Wright 2018).

Table 2
System Parameters

Parameter	Value
Spectral Fit Parameters	
$T_{\rm eff,1}$ (K)	2879 ± 37
$T_{\rm eff,2}$ (K)	2627 ± 71
$\log g_1$ (log cm s^{-2})	5.49 ± 0.02
$\log g_2$ (log cm s^{-2})	5.47 ± 0.04
$v \sin i_1$ (km s^{-1})	4.2 ± 1.7
$v \sin i_2$ (km s^{-1})	5.9 ± 2.0
$f_{2.3}$	0.65 ± 0.08
Orbit Fit Parameters	
P (days)	0.7106156 ± 0.0000002
K_1 (km s^{-1})	23.70 ± 0.05
K_2 (km s^{-1})	28.41 ± 0.06
$\sqrt{e} \sin\omega$	$0.086^{+0.009}_{-0.010}$
$\sqrt{e} \cos\omega$	$0.034^{+0.013}_{-0.014}$
v_0 (km s^{-1})	$+6.61 \pm 0.02$
M_0 (rad)	$1.98^{+0.14}_{-0.15}$
e	0.0088 ± 0.0017
ω (rad)	$1.20^{+0.15}_{-0.14}$
q	0.8340 ± 0.0017
σ_J (km s^{-1})	$-2.48^{+0.13}_{-0.12}$
Estimated Parameters	
Age (Gyr)	1–10
$T_{\rm eff,1}$ (K)	2395 ± 133
M_1 ($M_\odot$)	0.076–0.087
M_2 ($M_\odot$)	0.063–0.073
$R_{1,2}$ ($R_\odot$)	0.093–0.109
a (au)	0.0081–0.0084
	17–19 $R_{1,2}$
i (deg)	24.3 ± 0.6

$\chi^2_r = 2.7$ significantly better than the equivalent single-star model ($\chi^2_r = 7.6$). The component RVs in this epoch differ by 36.9 ± 0.3 km s^{-1}, more than 3 times the spectral resolution. Averaging over the several epochs of 2.3 μm measurements (Table 2), we find that the weaker lines emerge from a component that is $f_{2.3} = 0.65 \pm 0.08$ times as bright and 250 K cooler than the stronger line component, consistent with the expected ordering of secondary and primary. The model temperature for the primary, $T_{\rm eff} = 2879 \pm 37$ K, is somewhat warmer than the typical temperatures of M9 dwarfs (2370–2480 K; Stephens et al. 2009; Filippazzo et al. 2015; Dupuy & Liu 2017), and likely reflects model bias common to fits of spectral data over narrow wavelength ranges (see Rice et al. 2010). Both components have similar $\log g \approx 5.5$ (cgs), consistent with evolved UCDs. Both components also have similar $v \sin i$ s that are close to the resolution limit of the data (Hsu et al. 2021a). These $v \sin i$ values are similar to the $v \sin i = 4$ km s^{-1} reported in Reid et al. (2002), but significantly smaller than the 12.2 ± 3.0 km s^{-1} reported in Deshpande et al. (2012), which could be explained by line doubling. These results hold across all epochs, with component RV differences as high as 50 km s^{-1}.

4. Radial Velocity Time Series and Binary Orbital Fit

We measured the orbital parameters of LP 413-53 by fitting the primary and secondary RV measurements with the archival NIRSPEC J-band data and our acquired NIRSPEC K-band data. We used a two-component radial velocity orbit model to measure the orbital parameters of the RV time series:

$$\mathrm{RV_1} = K_1[e\cos\omega + \cos(T(t) + \omega)] + v_0 \quad (1)$$

$$\mathrm{RV_2} = -K_2\,[e\cos\omega + \cos(T(t) + \omega)] + v_0 = -\frac{K_1}{q}[e\cos\omega + \cos(T(t) + \omega)] + v_0. \quad (2)$$

Here, $\mathrm{RV}_{1,2}$ and $K_{1,2}$ are the radial velocities and RV semiamplitudes of the primary and secondary components, respectively; $q = M_2/M_1$ is the binary mass ratio; e is the orbital eccentricity; ω is the argument of periastron; v_0 is the systematic velocity; and $T(t)$ is the true anomaly of the orbit. The mean anomaly, $M = M_0 + 2\pi(t - t_0)/P$ with $t_0 = 59{,}952.24622$ MJD and P being the orbital period, is related to the true anomaly $T(t)$ through Kepler's equation, which we computed using the `kepler.py`[6] code. We also introduced an RV offset term for the J-band data relative to the K-band data, σ_J, to account for interband calibration differences, a common approach for analyzing multi-instrument RV time series (see Howard et al. 2014). To determine the best-fit orbital parameters and their uncertainties, we used an MCMC algorithm through the `emcee` package (Foreman-Mackey et al. 2013). Our log likelihood function $\mathcal{L}$ was defined as

$$\ln\mathcal{L} = -0.5 \times (\chi^2_1 + \chi^2_2 + \Sigma_i[\ln 2\pi\sigma^2_{1,i}] + \Sigma_i[\ln 2\pi\sigma^2_{2,i}]), \quad (3)$$

where $\sigma_{1,2}$ are the RV measurement uncertainties and $\chi^2_{1,2} = \Sigma_i[(\mathrm{RV_{measure,i}} - \mathrm{RV_{model,i}})/\sigma_i]^2$ for the primary and secondary components, respectively. We chose a basis set of P, K_1, K_2, $\sqrt{e}\sin\omega$, $\sqrt{e}\cos\omega$, v_0,M_0, and σ_J to simultaneously fit the RV time series of both components, following Ford (2005). We excluded from our fit the first four RV measurements on 2022 December 2, and the three epochs of 59,952.43355, 59,952.43702, and 59,952.44147 MJD on 2023 January 8, as the unresolved RVs at these epochs are likely less reliable, although our result is largely consistent with these measurements. We used 100 chains of 400,000 steps each, with the first 25% of each chain discarded as burn-in. The chains converged in the first few hundred steps, with an integrated autocorrelation scale of 370 steps.

The resulting best-fit orbit parameters and their uncertainties are listed in Table 2, and the best-fit orbit with an overall reduced $\chi^2_r = 2.5$ is compared to the RV time series in Figure 3. Our observations sample over half of the orbit phase, and notably cover both oppositional points when the sources are at maximum RV separation. The best-fit period of the system of 0.7106156 ± 0.0000002 days is constrained to better than 0.02 s precision, although there may be unaccounted-for systematic errors due to our incomplete phase coverage. This period is 4 times shorter than that of USCO J1616−2512, making LP 413-53 the shortest-period UCD binary currently known. We find a small but nonzero eccentricity, although our orbit sampling may bias the uncertainties for this parameter and we cannot rule out a fully circular orbit due to tidal

[6] https://github.com/dfm/kepler.py

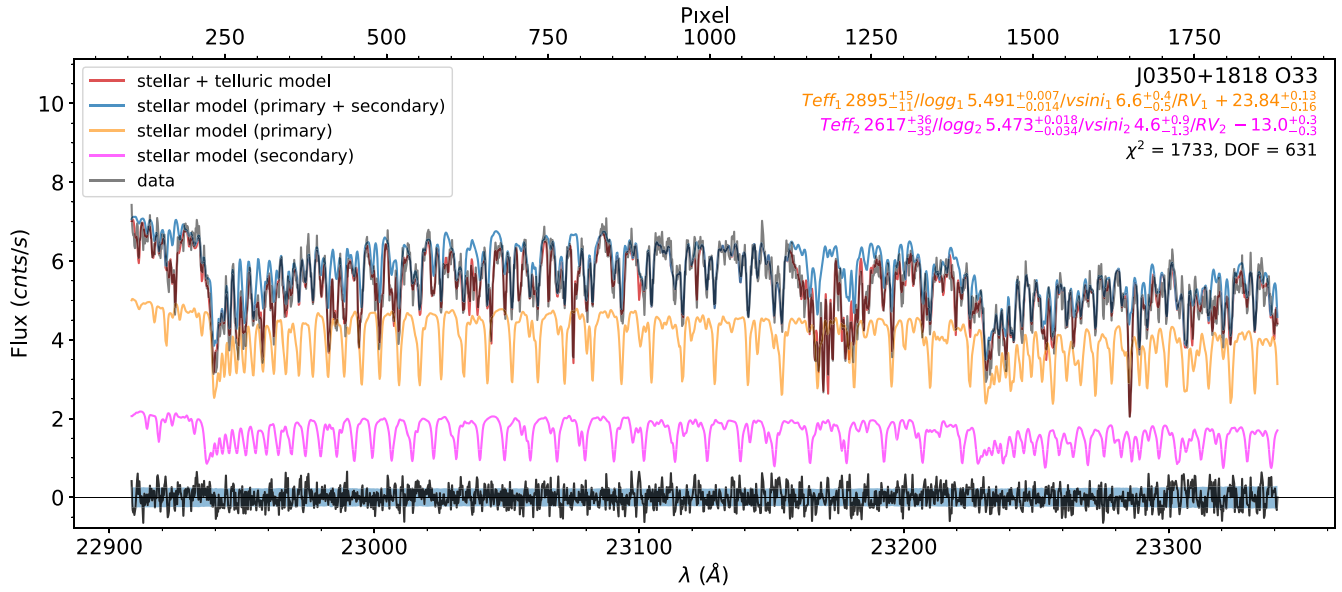

Figure 2. Forward-model fit to the 2.29–2.33 μm (order 33) Keck/NIRSPEC spectrum of LP 413-53 obtained on 2022 March 13 at 05:02:59.43 UT (59,651.20898 MJD; black line). The forward model consists of primary (orange) and secondary (magenta) spectra, with the combined spectrum (blue) modulated by telluric absorption (red). The residual (data − model) and uncertainty are depicted by the black line and gray-shaded region along the bottom, respectively. The legend provides the final fit parameters for component temperatures ($T_{\rm eff}$ in K), log surface gravities ($\log g$ in log cm s^{-2}), rotational velocities ($v \sin i$ in km s^{-1}), and radial velocities (RV in km s^{-1}) with their uncertainties, as well as the best-fit χ^2 and degrees of freedom (DOF).

circularization (see below). The relative amplitudes of the primary and secondary RV curves allow us to directly measure the system mass ratio as $q = M_2/M_1 = K_1/K_2 = 0.8340 \pm 0.0017$, which is qualitatively consistent with the unequal line depths and inferred $T_{\rm eff}$s of the component spectra. We note that while our σ_J is relatively large ($-2.48^{+0.13}_{-0.12}$ km s^{-1}), it is a subpixel shift, and we regard the K-band center-of-mass motion to be the reliable measure. For completeness, we also determined orbital parameters by fitting the K-band data alone. We found consistent orbital parameters of $P = 0.710623 \pm 0.000002$ days (note the 10 times larger uncertainty), $K_1 = 23.62 \pm 0.05$ km s^{-1}, $K_2 = 28.30 \pm 0.07$ km s^{-1}, $q = 0.8345 \pm 0.0017$, $v_0 = 6.61 \pm 0.02$ km s^{-1}, and $e = 0.0103 \pm 0.0017$; slightly different values of $M_0 = 1.52^{+0.18}_{-0.19}$ rad and $\omega = 1.65^{+0.19}_{-0.18}$ rad; and the same $\chi^2_r = 2.5$.

5. Discussion

The short orbital period of LP 413-53 makes it a likely candidate for eclipsing, depending on its physical separation and component radii, with the latter depending on the system age. We reevaluated the kinematic evidence of Hyades association membership by combining our systematic RV with Gaia DR3 astrometry, which yields a Galactic heliocentric velocity of $(U, V, W) = (-17.52 \pm 0.05, -24.68 \pm 0.11, +12.43 \pm 0.07)$ km s^{-1}. The velocity and position of the LP 413-53 system exclude membership in the Hyades, and in 26 other young, nearby clusters and associations, based on the BANYAN Σ web tool[7] (Gagne et al. 2018). The (occasionally) strong magnetic activity of LP 413-53 does not provide a firm constraint on the age of the system given the long magnetic activity lifetimes of very-low-mass stars (West et al. 2008), particularly binaries (Morgan et al. 2012). We therefore assume for the rest of this analysis that the components of LP 413-53 are low-mass stars with ages $\gtrsim$1 Gyr.

Component masses and radii were estimated from evolutionary models assuming that the combined-light M9 optical classification of the system reflects the primary component. We used the spectral type to $T_{\rm eff}$ relation from Filippazzo et al. (2015) to estimate a primary $T_{\rm eff} = 2395 \pm 133$ K, which is consistent to fits of broadband photometry to stellar models (2334^{+32}_{-24} K using stellar models from Husser et al. 2013). For an age of 1–10 Gyr, this temperature corresponds to a mass of 0.076–0.087 $M_\odot$ and radius[8] of 0.091–0.101 $R_\odot$ using the Burrows et al. (2001) models and 0.076–0.086 $M_\odot$ and 0.098–0.109 $R_\odot$ using the Baraffe et al. (2003) models. Choosing the outer ranges encompassing these values, our inferred mass ratio implies a secondary mass of 0.063–0.073 $M_\odot$, making it a possible brown dwarf.[9] These values yield a total system mass of 0.14–0.16 $M_\odot$, which combined with the period implies a semimajor axis $a = 0.0081$–0.0084 au or 17–19 stellar radii. We can further estimate the system inclination from the expected primary RV amplitude given these parameters:

$$K_1 = \frac{2\pi a}{P} \frac{q}{1+q} \frac{\sin i}{\sqrt{1-e^2}} \approx 57.5 \text{ km/s } \sin i. \quad (4)$$

Comparing this value to our observed $K_1 = 23.7$ km s^{-1} yields an estimated inclination angle of 24° and a corresponding projected separation on the sky of 7–8 stellar radii at closest approach. Thus, it is unlikely that this system will eclipse assuming the estimated component parameters are accurate, although observational confirmation of this assessment is warranted. We note that LP 413-53 is too faint for TESS monitoring and was not targeted with Kepler/*K2*.

[7] https://www.exoplanetes.umontreal.ca/banyan/banyansigma.php

[8] We are not taking into account 10%–20% radius inflation that is well-documented among very-low-mass stars (Kesseli et al. 2018).

[9] The lower range of secondary mass is consistent with the absence of Li I absorption in combined-light optical spectra (Reid et al. 1999).

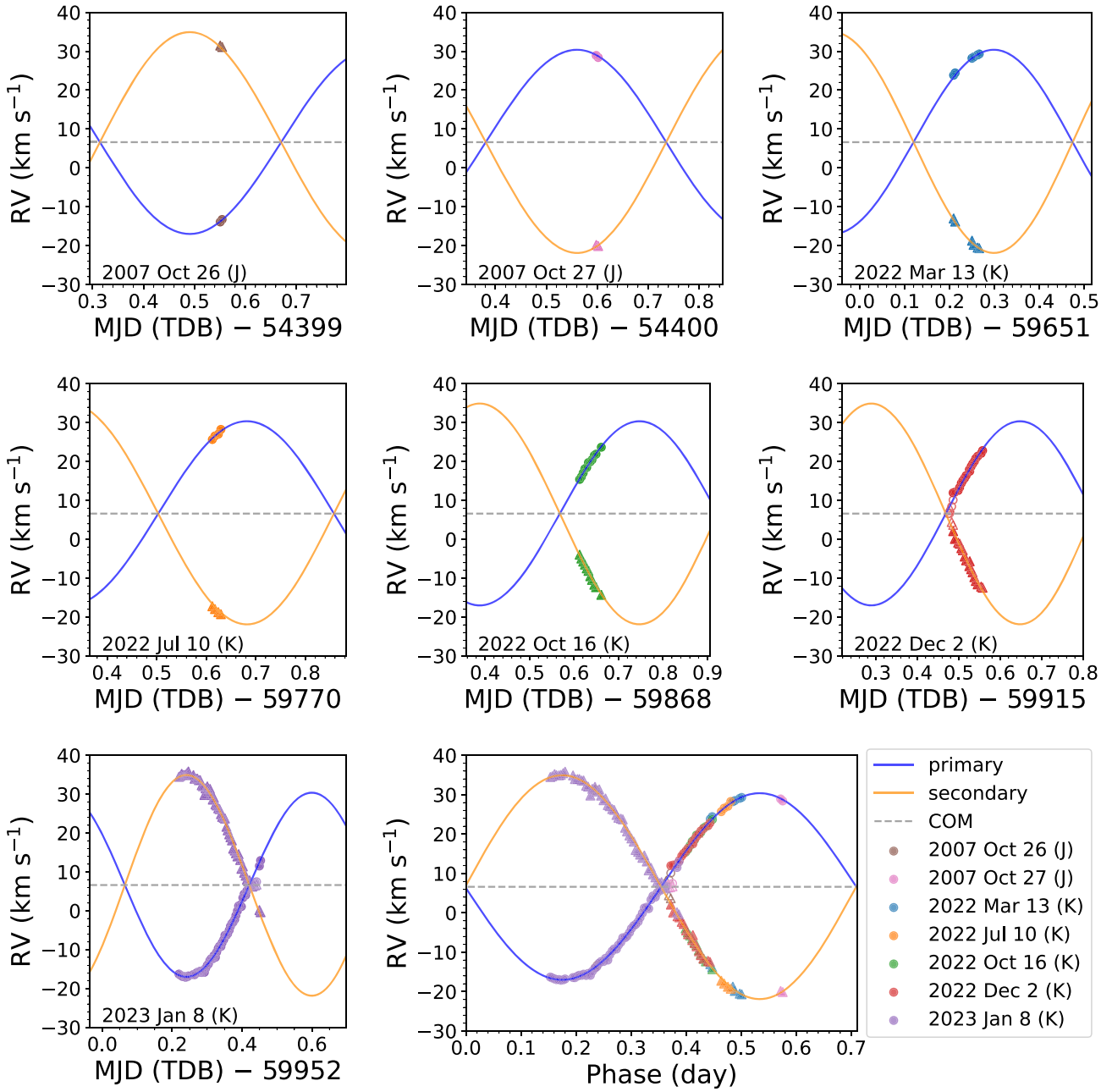

Figure 3. Radial velocity measurements for primary (circles) and secondary (triangles) components for individual UT epochs 2007 October 26, 2007 October 27, and 2022 March 13 (top row); 2022 July 10, 2022 October 16, and 2022 December 2 (middle row); and 2023 January 8 (bottom left), and the phase-folded RV curve (bottom right). Measurement uncertainties are smaller than the symbol size. In each panel, the best-fit orbit indicating primary (blue lines) and secondary (orange lines) RVs are indicated, as well as the center-of-mass (systematic) RV (gray dashed lines). The measurements from *J*-band data on 2007 October 26 and 2007 October 27 shown here have been corrected for the RV offset term σ_J. Four epochs in 2022 December 2 and three epochs in 2023 January 8 were excluded from the orbit fit due to their unresolved spectra (open circles); these are nevertheless included in the phase-folded RV curve (see Section 4).

While the estimated physical properties of the components of this system indicate that they do not currently come into close physical contact, this may not have been the case if the system formed at its current separation. The pre-main-sequence (ages $\sim$ 1 Myr) radii of very-low-mass stars are several times larger than their evolved configurations (Burrows et al. 2001; Baraffe et al. 2003; Stassun et al. 2006), bringing the components to near contact at early ages. Like more massive short-period stellar binaries, this system likely underwent orbital decay from an initially wider separation via angular momentum loss through tidal friction and magnetized winds (Stepien 1995). Alternately, LP 413-53 could have formed as part of an unstable triple or higher-order system, with the third component carrying away angular momentum from the now hardened pair. Indeed, several close UCD pairs, including SPEC 1510−2828AB (Triaud et al. 2020) and SDSS J0006−0852AB (Burgasser et al. 2012) are found in (presumed stable) hierarchical

triples. In the case of LP 413-53, the absence of a comoving companion within 1° (0.6 pc) would require this component to be fully ejected from the system. Both cases are expected to produce a low eccentricity, synchronously rotating binary given the short tidal circularization ($\sim 2 \times 10^5$ yr) and synchronization ($\sim 3 \times 10^3$ yr) timescales for fully convective stars at this separation (Zahn 1977; Fleming et al. 2019). The corresponding synchronized equatorial rotational velocity, ~ 7 km s^{-1} for a fully evolved low-mass star, consistent with projected $v \sin i \sim 3$ km s^{-1} if the spin axis is aligned with the orbital plane axis, is consistent with the observed values given our detection limits. Higher-resolution data could provide a second constraint on the orbit geometry assuming spin–orbit alignment, or alternately test that alignment and potentially differentiate between formation via slow tidal dissipation or three-body interaction.

Finally, we note that while no physical interaction is present in this system, magnetospheric interaction, even if indirect, likely is. The radio magnetospheres of low-mass stars extend 1–3 stellar radii beyond the photosphere (Alef et al. 1997; Ravi et al. 2011; Burgasser et al. 2013), and can be further distorted by the gravitational potential of the system. Such interaction may explain the highly variable Hα measurements reported in the literature, and warrants optical spectral monitoring to search for phased emission as seen in other short-period M dwarf systems (see Davenport et al. 2013). We note that the long convective timescales of the lowest-mass stars ($\gtrsim$100 day; Wright et al. 2011) imply that both components will remain in the saturated regime for magnetic emission ($R_o < 10^{-2}$; Newton et al. 2017), and are thus likely to continue to lose angular momentum through dual magnetized winds.

The authors thank observing assistants Heather Hershley, Anthony Connors, Julie Renaud-Kim, and Matthew Wahl, and supporting astronomers James Lyke, Rosalie McGurk, Percy Gomez, and Gregory Doppmann for their help in obtaining our Keck/NIRSPEC observations on 2022 March 13 (UT), 2022 July 10 (UT), 2022 October 16 (UT), 2022 December 2 (UT), and 2023 January 8 (UT). The authors also like to thank Erik Petigura and Dakotah Tyler for their generous swap in the Keck/NIRSPEC observation on 2022 October 16. The authors thank the anonymous referee for the valuable review that has improved the original manuscript. Data presented herein were obtained at the W. M. Keck Observatory, which is operated as a scientific partnership among the California Institute of Technology, the University of California, and the National Aeronautics and Space Administration. The Observatory was made possible by the generous financial support of the W. M. Keck Foundation. This research has made use of the Keck Observatory Archive (KOA), which is operated by the W. M. Keck Observatory and the NASA Exoplanet Science Institute (NExScI), under contract with the National Aeronautics and Space Administration. The authors recognize and acknowledge the significant cultural role and reverence that the summit of Maunakea has with the indigenous Hawaiian community, and that the W. M. Keck Observatory stands on Crown and Government Lands that the State of Hawai'i is obligated to protect and preserve for future generations of indigenous Hawaiians. Portions of this work were conducted at the University of California, San Diego, which was built on the unceded territory of the Kumeyaay Nation, whose people continue to maintain their political sovereignty and cultural traditions as vital members of the San Diego community.

Facility: Keck:II (NIRSPEC).

Software: `Astropy` (Astropy Collaboration et al. 2018), `BANYAN Σ` (Gagne et al. 2018), `SMART` (Hsu et al. 2021a), `SPLAT` (Burgasser 2017).

ORCID iDs

Chih-Chun Hsu https://orcid.org/0000-0002-5370-7494
Adam J. Burgasser https://orcid.org/0000-0002-6523-9536
Christopher A. Theissen https://orcid.org/0000-0002-9807-5435

References

Alef, W., Benz, A. O., & Guedel, M. 1997, A&A, 317, 707
Allard, F., Homeier, D., & Freytag, B. 2012, RSPTA, 370, 2765
Astropy Collaboration, Price-Whelan, A. M., Sipőcz, B. M., et al. 2018, AJ, 156, 123
Baraffe, I., Chabrier, G., Barman, T. S., Allard, F., & Hauschildt, P. H. 2003, A&A, 402, 701
Bardalez Gagliuffi, D. C., Burgasser, A. J., Gelino, C. R., et al. 2014, ApJ, 794, 143
Basri, G., & Martin, E. L. 1999, AJ, 118, 2460
Belokurov, V., Penoyre, Z., Oh, S., et al. 2020, MNRAS, 496, 1922
Blake, C. H., Charbonneau, D., & White, R. J. 2010, ApJ, 723, 684
Bouy, H., Brandner, W., Martín, E. L., et al. 2003, AJ, 126, 1526
Burgasser, A. J. 2017, ASInC, 14, 7
Burgasser, A. J., Cruz, K. L., Cushing, M., et al. 2010, ApJ, 710, 1142
Burgasser, A. J., Luk, C., Dhital, S., et al. 2012, ApJ, 757, 110
Burgasser, A. J., Melis, C., Zauderer, B. A., & Berger, E. 2013, ApJL, 762, L3
Burgasser, A. J., Reid, I. N., Siegler, N., et al. 2007, in Protostars and Planets V, ed. B. Reipurth, D. Jewitt, & K. Keil (Tucson, AZ: Univ. Arizona Press), 427
Burrows, A., Hubbard, W. B., Lunine, J. I., & Liebert, J. 2001, RvMP, 73, 719
Carmichael, T. W., Quinn, S. N., Zhou, G., et al. 2021, AJ, 161, 97
Close, L. M., Siegler, N., Freed, M., & Biller, B. 2003, ApJ, 587, 407
Cruz, K. L., & Reid, I. N. 2002, AJ, 123, 2828
Davenport, J. R. A., Becker, A. C., West, A. A., et al. 2013, ApJ, 764, 62
Deshpande, R., Martín, E. L., Montgomery, M. M., et al. 2012, AJ, 144, 99
Dimitrov, D. P., & Kjurkchieva, D. P. 2010, MNRAS, 406, 2559
Duchêne, G., & Kraus, A. 2013, ARA&A, 51, 269
Dupuy, T. J., & Liu, M. C. 2017, ApJS, 231, 15
Eastman, J., Siverd, R., & Gaudi, B. S. 2010, PASP, 122, 935
Filippazzo, J. C., Rice, E. L., Faherty, J., et al. 2015, ApJ, 810, 158
Fleming, D. P., Barnes, R., Davenport, J. R. A., & Luger, R. 2019, ApJ, 881, 88
Fontanive, C., Biller, B., Bonavita, M., & Allers, K. 2018, MNRAS, 479, 2702
Ford, E. B. 2005, AJ, 129, 1706
Foreman-Mackey, D., Hogg, D. W., Lang, D., & Goodman, J. 2013, PASP, 125, 306
Gagné, J., Mamajek, E. E., Malo, L., et al. 2018, ApJ, 856, 23
Gaia Collaboration, Vallenari, A., & Brown, A. G. A. 2022, arXiv:2208.00211
Gizis, J. E., Monet, D. G., Reid, I. N., et al. 2000, AJ, 120, 1085
Gizis, J. E., Reid, I. N., Knapp, G. R., et al. 2003, AJ, 125, 3302
Goldman, B., Röser, S., Schilbach, E., et al. 2013, A&A, 559, A43
Howard, A. W., Marcy, G. W., Fischer, D. A., et al. 2014, ApJ, 794, 51
Hsu, C.-C., Burgasser, A. J., Theissen, C. A., et al. 2021a, ApJS, 257, 45
Hsu, C.-C., Theissen, C., Burgasser, A., & Birky, J. 2021b, SMART: The Spectral Modeling Analysis and RV Tool, Zenodo, doi:10.5281/zenodo.4765258
Husser, T.-O., Wende-von Berg, S., Dreizler, S., et al. 2013, A&A, 553, A6
Kanodia, S., & Wright, J. 2018, RNAAS, 2, 4
Kesseli, A. Y., Muirhead, P. S., Mann, A. W., & Mace, G. 2018, AJ, 155, 225
Kiman, R., Schmidt, S. J., Angus, R., et al. 2019, AJ, 157, 231
Lodieu, N. 2020, MmSAI, 91, 84
Lodieu, N., Alonso, R., González Hernández, J. I., et al. 2015, A&A, 584, A128
Maceroni, C., & Rucinski, S. M. 1997, PASP, 109, 782
McLean, I. S., Becklin, E. E., Bendiksen, O., et al. 1998, Proc. SPIE, 3354, 566
McMath, R. R., Mohler, O. C., & Goldberg, L. 1949, ApJ, 109, 17
Moehler, S., Modigliani, A., Freudling, W., et al. 2014, A&A, 568, A9
Morgan, D. P., West, A. A., Garcés, A., et al. 2012, AJ, 144, 93

Nefs, S. V., Birkby, J. L., Snellen, I. A. G., et al. 2012, MNRAS, 425, 950
Newton, E. R., Irwin, J., Charbonneau, D., et al. 2017, ApJ, 834, 85
Ravi, V., Hallinan, G., Hobbs, G., & Champion, D. J. 2011, ApJL, 735, L2
Reid, I. N., Kirkpatrick, J. D., Liebert, J., et al. 1999, ApJ, 521, 613
Reid, I. N., Kirkpatrick, J. D., Liebert, J., et al. 2002, AJ, 124, 519
Rice, E. L., Barman, T., Mclean, I. S., Prato, L., & Kirkpatrick, J. D. 2010, ApJS, 186, 63
Ricker, G. R., Vanderspek, R., Winn, J., et al. 2016, Proc. SPIE, 9904, 99042B
Sahlmann, J., Burgasser, A. J., Bardalez Gagliuffi, D. C., et al. 2020, MNRAS, 495, 1136
Smart, R. L., Marocco, F., Sarro, L. M., et al. 2019, MNRAS, 485, 4423
Stassun, K. G., Mathieu, R. D., & Valenti, J. A. 2006, Natur, 440, 311
Stephens, D. C., Leggett, S. K., Cushing, M. C., et al. 2009, ApJ, 702, 154
Stepien, K. 1995, MNRAS, 274, 1019
Theissen, C. A., Konopacky, Q. M., Lu, J. R., et al. 2022, ApJ, 926, 141
Tran, H. D., Cohen, R., Colson, A., et al. 2016, Proc. SPIE, 9910, 99102E
Tran, H. D., Holt, J., Goodrich, R. W., et al. 2014, Proc. SPIE, 9152, 91522I
Triaud, A. H. M. J., Burgasser, A. J., Burdanov, A., et al. 2020, NatAs, 4, 650
West, A. A., Hawley, S. L., Bochanski, J. J., et al. 2008, AJ, 135, 785
Wright, N. J., Drake, J. J., Mamajek, E. E., & Henry, G. W. 2011, ApJ, 743, 48
Zahn, J. P. 1977, A&A, 57, 383
Zhang, B., Qian, S.-B., Zhi, Q.-J., et al. 2019, PASP, 131, 034201